Reduction of the loads on a cylinder undergoing harmonic in-line motion

Osama A. Marzouk and Ali H. Nayfeh

Reduction of the loads on a cylinder undergoing harmonic in-line motion

Osama A. Marzouk[a)] and Ali H. Nayfeh
Department of Engineering Science and Mechanics (Mail Code 0219), Virginia Polytechnic Institute and State University, Blacksburg, Virginia 24061, USA

We use the finite-difference computational fluid dynamics method to study in detail the flow field around a circular cylinder in a uniform stream while undergoing in-line harmonic motion. For a given motion amplitude, there exists a critical forcing frequency below which the lift and drag can be period-n, quasiperiodic, or chaotic. Similarly, for a given frequency, there exists a critical amplitude below which the lift and drag can be period-n, quasiperiodic, or chaotic. Above these critical conditions, the lift and drag are synchronous with the forcing. The lift nearly vanishes and the mean drag drops and saturates at a value that is independent of the driving frequency, whereas the oscillatory drag quadratically depends on it. We relate these features to changes in the wake and the surface-pressure distribution. We examine the influence of the Reynolds number on these critical frequency and amplitude. Second- and higher-order spectral analyses show remarkable changes in the linear and quadratic coupling between the lift and drag when synchronization takes place; it destroys the two-to-one coupling between them in the cases of no motion and synchronization due to cross-flow motion. © *2009 American Institute of Physics.* [DOI: 10.1063/1.3210774]

I. INTRODUCTION

The development of vortices and unsteady flow motion in the wake of a body in a uniform stream is a classical problem in fluid mechanics, which can be observed particularly in offshore structures, such as risers, spar platforms, fixed platforms, tension leg platforms, and jack up rigs. If the body is not fixed, one or more of several motion types can occur,[1] including translational vortex-induced vibrations, torsional vortex-induced vibrations, galloping, airfoil flutter, multibody structure wake galloping, and breathing oscillations.

The continuously generated vortices have direct effect on the exerted force on the body. This force can be decomposed into two components: lift (cross-flow component) and drag (in-line component). These components depend on the body geometry. We consider here a circular cylinder due to its simplicity and its common use in industrial applications. Moreover, the wake behind a circular cylinder is simpler than those behind noncircular cylinders, which allows more informative analysis with less number of geometric parameters. Furthermore, unlike square cylinders, galloping does not occur for a circular cylinder.[2,3]

The Strouhal number (S_K) associated with the von Kármán vortex street is the nondimensional frequency at which two counter-rotating vortices are repeatedly shed in the wake of a bluff body (a cylinder is a special case) restrained from any type of motion in a uniform stream; it is a characteristic of the wake of that body. When a cylinder is driven in the cross-flow direction (perpendicular to the incoming stream and to its span) with a nondimensional frequency S_M close to S_K, the nondimensional vortex shedding frequency S_V is synchronized at the forcing frequency S_M,[4–7]

thus shedding is entrained by the cylinder motion. As a consequence, the lift is synchronized at S_M. Similar to the case of a fixed cylinder,[8–10] the drag frequency is twice the lift frequency and is synchronized at $2S_M$. On the other hand, when a cylinder is forced to oscillate in the in-line direction (parallel to the incoming stream) with a nondimensional frequency S_M around twice S_K, shedding is synchronized at $\frac{1}{2}S_M$.[11–13] The synchronization phenomenon also occurs when a cylinder is constrained to oscillate in either the cross-flow or in-line directions by a spring and a dashpot.[14,15]

The difference in the range of synchronization frequencies in the two cases is explained by the phasing between the moving cylinder and the synchronized shedding.[16] For harmonic motion in the in-line direction with two alternating vortices being shed periodically, either shedding event of the top and bottom vortex is always promoted when shedding occurs at half the motion frequency. However, only every other shedding event will be promoted if the motion frequency is equal to the shedding frequency. The situation is altered in the case of harmonic motion in the cross-flow direction, where shedding is enhanced when it occurs at the motion frequency but is partly opposed if it occurs at half the motion frequency.

Studies of a one-degree-of-freedom moving cylinder usually consider the cross-flow motion with the in-line motion being restrained. Many of these published studies do not indicate the motion direction in the title because it is by default the cross-flow direction.[17–19] There is disagreement on the importance of the in-line cylinder motion on its wake and dynamics. Some studies show that the induced in-line motions are one order of magnitude smaller than the cross-flow motions,[20,21] others emphasize the importance of the induced in-line motions even though they are small, and others show that they can be comparable to the cross-flow mo-

---

a)Electronic mail: omarzouk@vt.edu.

tions, depending on the cylinder density[22,23] or its nondimensional natural frequency.[24]

Tanida *et al.*[12] carried out experiments on a one-degree-of-freedom circular cylinder oscillating harmonically in the in-line direction at the Reynolds numbers Re=80 and 4000. The first part of their study considered a single circular cylinder oscillating in a uniform stream, whereas the second part was dedicated to the case of a circular cylinder oscillating in the wake of another cylinder (i.e., tandem arrangement). In both parts, they measured the lift and drag on the oscillating cylinder. In the first case, the cylinder was made to oscillate sinusoidally with a prescribed amplitude that is 14% of its diameter (the amplitude was 4.2 mm and the diameter was 30 mm) and frequencies varying from below to above $2S_K$. Each experiment corresponded to a single frequency. Individual experiments lasted for at least 20 s, which was long enough for the steady state to be achieved. The working liquid was oil for Re=80 and water for Re=4000. They observed synchronization for both configurations. They also reported that the fluctuating lift "vanishes" occasionally at Re=4000, where its magnitude drops to very small levels when the forcing frequency is around twice S_K. They related this lift suppression to a positive aerodynamic damping induced by the cylinder motion, which they described as being "stable" in this condition, and to the work done by the drag force. We show this lift suppression numerically at other Reynolds numbers. We then enhance their explanation by examining variations of multiple flow variables and their characteristics, such as the vortex structure, the lift and drag harmonics and their coupling, and the phase between the synchronous drag and motion. We consider a broad range of S_M that is not limited to the synchronous range.

Kim and Williams[25] measured the lift and drag on a cylinder undergoing harmonic motion in air at Re=15 200 and studied the nonlinear coupling between them. The cylinder diameter was 50.8 mm and its length was 610 mm. A printed circuit motor connected to a Scotch-yoke mechanism was used to control the motion. The main part of the experiment was conducted at a constant motion amplitude of 3.5% of the diameter, which is very small. Also, the motion frequency was $0.8S_K$, which is far below the synchronization range. They revealed interesting facts about the nonlinear interaction between the lift and drag and explained the structure of their measured power spectra.

In this study, we consider a circular cylinder undergoing a one-degree-of-freedom harmonic motion in the in-line direction in a uniform stream at different Re. The motion induces a mechanical perturbation in the shear layer. We limit ourselves to the influence of the forcing frequency on the dynamics of the flow and the exerted forces. We compute the velocities and pressure and pay special attention to the synchronization that occurs near twice S_K. Several differences exist between this synchronization and the one that occurs when the cylinder is fixed or driven in the cross-flow direction around S_K. We use different analysis techniques to examine and highlight these differences and relate them to changes in the vortex shedding and the surface pressures.

II. APPROACH

All variables are made nondimensional using the cylinder diameter $\hat{D}$ as a reference length, the incoming far-field velocity $\hat{U}_\infty$ as a reference velocity, and $\hat{U}_\infty/\hat{D}$ as a reference time. For the cylinder motion, we let

$$\xi(t) = A_x \sin(2\pi S_M t), \tag{1}$$

where ξ is the displacement and A_x and S_M are the nondimensional amplitude and cyclic frequency of the cylinder motion, respectively.

The velocity and pressure fields are governed by the two-dimensional, unsteady Navier–Stokes equations,

$$\frac{\partial u}{\partial x} + \frac{\partial v}{\partial y} = 0,$$

$$\frac{\partial u}{\partial t} = -(u - u_g)\frac{\partial u}{\partial x} - (v - v_g)\frac{\partial u}{\partial y} - \frac{\partial p}{\partial x} + \frac{1}{\text{Re}}\left(\frac{\partial^2 u}{\partial x^2} + \frac{\partial^2 u}{\partial y^2}\right),$$

$$\tag{2}$$

$$\frac{\partial v}{\partial t} = -(u - u_g)\frac{\partial v}{\partial x} - (v - v_g)\frac{\partial v}{\partial y} - \frac{\partial p}{\partial y} + \frac{1}{\text{Re}}\left(\frac{\partial^2 v}{\partial x^2} + \frac{\partial^2 v}{\partial y^2}\right),$$

where u and v are the x-component and y-component of the fluid velocity, u_g and v_g are the x-component and y-component of the grid speed, and p is the pressure. Equations (2) are first Reynolds-averaged and the Baldwin–Barth eddy-viscosity model is used to account for the unresolved turbulent scales. The resulting equations are then rewritten in body-fitted coordinates ξ and η, instead of x and y, which are aligned with the boundaries.[26,27] The differential equations are discretized using central second-order differences for the viscous terms, an upwind flux-difference splitting scheme for the convective terms, and a second-order implicit backward Euler scheme for the local derivatives. The numerical fluxes are calculated at the midcell location. A colocated arrangement of the primitive variables is used, where the discretized velocities and pressure fields are defined at the same grid points. For efficient calculations, the orthogonal viscous terms are treated implicitly, whereas the nonorthogonal terms (which arise due to nonorthogonality in the grid lines) are treated explicitly by moving them to the right-hand side of the algebraic system. For a fixed cylinder, the grid is orthogonal and the nonorthogonal viscous terms are analytically equal to zero. On the other hand, the in-line motion causes deformations in the grid, but the nonorthogonality is small as can be seen in Fig. 1. Therefore, these nonorthogonal terms are not significant and their explicit treatment is a minor issue. We performed grid sensitivity checks and confirmed that higher resolutions do not cause important changes in the simulation results. A no-slip boundary condition is applied at the cylinder surface. At the far-field inflow boundary, a uniform horizontal stream is applied for the velocities (i.e., $u = U_\infty = 1$ and $v = V_\infty = 0$), whereas the pressure is extrapolated. At the far-field outflow boundary, the pressure is specified ($p = P_\infty = 1$), whereas the velocities are extrapolated. Figure 1 shows a portion of the cylinder at its farthest downstream and upstream locations. The outer shape
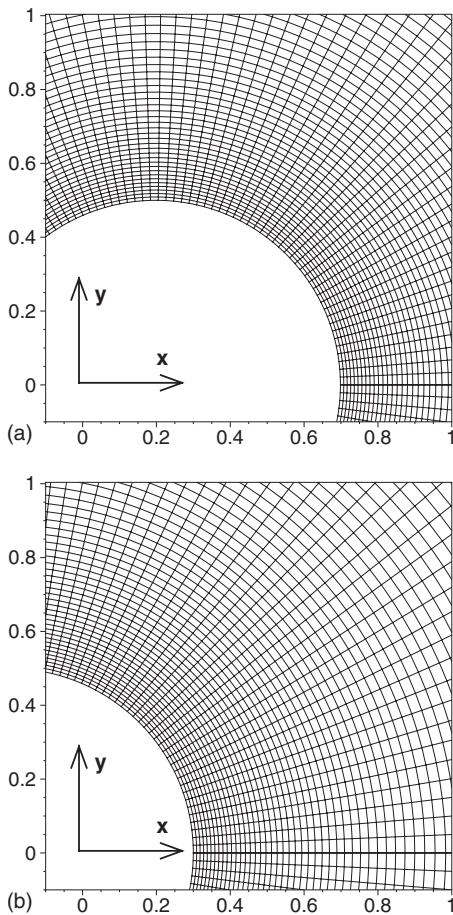
FIG. 1. Partial views of the cylinder and grid at the instants of (i) maximum displacement and (ii) minimum displacement.

of the computational region is a nondeforming circle with a nondimensional radius equal to 25. The equations are solved iteratively, and the iteration is stopped when the maximum absolute residual of the continuity equation over all grid points is less than 10^{-4} or after 12 iterations. The problem is solved on a Silicon Graphics, Inc. (SGI) machine with 1.6 GHz processor speed and 512 GB memory. Each time step takes about 1.18 s of CPU time. The nondimensional time step is 0.05.
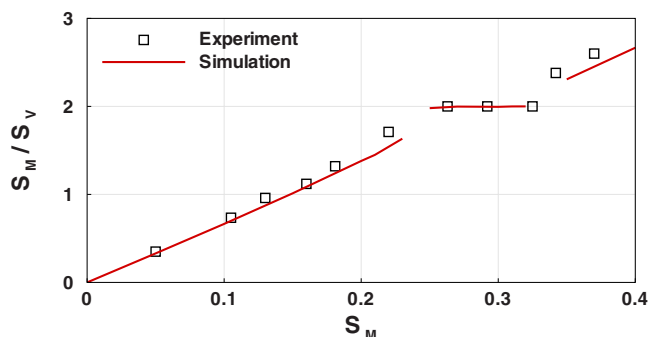

FIG. 2. (Color online) Comparison between our simulations and the measurements of Tanida *et al.* (Ref. 12) for the variation of the forcing-to-shedding frequency ratio S_M / S_V with the nondimensional forcing frequency S_M for a cylinder oscillating in-line at Re=80 with nondimensional amplitude A_x=0.14.
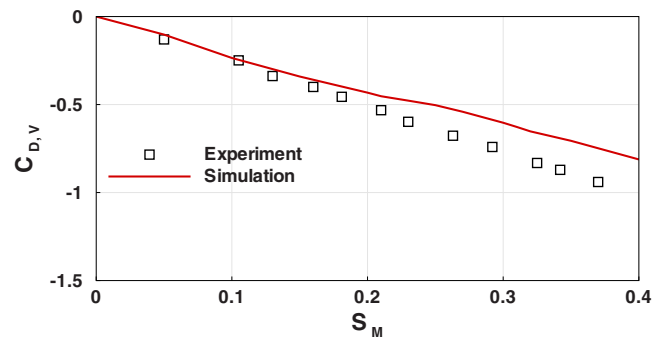

FIG. 3. (Color online) Comparison between our simulations and the measurements of Tanida *et al.* (Ref. 12) for the variation of the drag component in phase with velocity $C_{D,V}$ with the nondimensional forcing frequency S_M for a cylinder oscillating in-line at Re=80 with A_x=0.14.

We start by comparing our simulations with the reported experimental data of Tanida *et al.*[12] The experiments were conducted in oil at Re=80, with an in-line motion amplitude equal to 14% of the cylinder diameter. To reduce three-dimensional effects, they took measurements at the central section of the test cylinder. In Fig. 2, the ratio of the shedding frequency to the forcing frequency S_V / S_M is plotted as a function of S_M. In addition to the good agreement between the simulations and the measurements, this figure shows also one type of synchronization at this Re and A_x, in which S_V (which is also the fundamental lift frequency) is equal to $\frac{1}{2}S_M$. Further analysis of the simulation results of the synchronous lift and drag showed that C_D is synchronous at S_M. Therefore, there is a quadratic coupling between the synchronous lift and drag as in the case of no motion and the case of synchronization due to cross-flow motion. We focus in this study on another type of synchronization due to in-line motion in which the lift is synchronous at S_M and its amplitude is reduced to very low levels. Figure 3 shows the component of the drag coefficient C_D in phase with the velocity of the in-line motion, which we denote by $C_{D,V}$, as a function of S_M. Again, there is good agreement between our simulations and the measurements. Figure 4 compares variations of the root mean square (rms) of the calculated lift coefficient C_L with S_M to the measured one. As mentioned before, the synchronous C_L is not reduced at this very low Re.
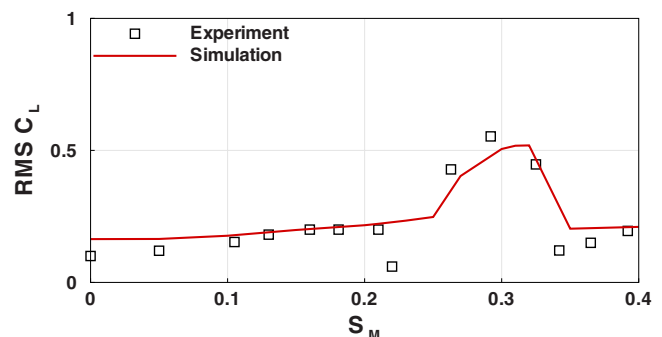

FIG. 4. (Color online) Comparison between our simulations and the measurements of Tanida *et al.* (Ref. 12) for the variation of rms C_L with the nondimensional forcing frequency S_M for a cylinder oscillating in-line at Re=80 with A_x=0.14.
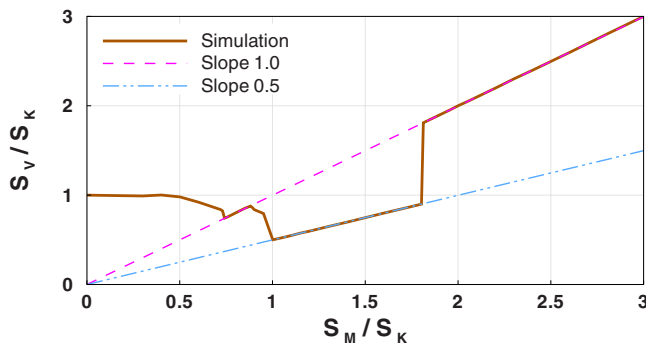
FIG. 5. (Color online) Variation of the shedding-to-Strouhal frequency ratio S_V/S_K with the forcing-to-Strouhal frequency ratio S_M/S_K. Postsynchronization region in the simulation results is indicated by a slope of unity.

III. RESULTS AND DISCUSSION

A. Lift and drag

We investigate several flow properties over a wide range of mechanical frequencies S_M while fixing the amplitude of motion A_x at 0.20. This value allows us to compare the flow features for this case with those obtained for a cylinder with cross-flow motion at the same amplitude and Re.[28] The majority of the results correspond to Re=500; the others correspond to Re=300. Synchronization is illustrated in Fig. 5, which shows the ratio S_V/S_K as a function of the ratio S_M/S_K. When $S_M \approx 2S_K$, vortex shedding is synchronized at S_M. Hence the graph of S_V/S_K with S_M/S_K is a straight line with unity slope; it starts at the critical value $S_M/S_K=1.81$ and extends to $S_M/S_K=3.33$. Beyond this value, the synchronous shedding bifurcates and becomes nonsynchronous with less regular pattern and with an asymmetric lift. We refer to this range of S_M as postsynchronization compared to presynchronization when S_M is below the critical value. This range is in contrast to the range $0.81 < S_M/S_K < 1.05$ for the case of cross-flow motion at the same amplitude and Re. So, the synchronization range here is not just shifted, but it is also broadened. It should be mentioned that the postsynchronization range is preceded by a region in the presynchronization range where the shedding occurs at half S_M. Therefore, one can describe vortex shedding as being synchronized at $\frac{1}{2}S_M$ as reported in other studies.[12,32] However, because we want

to focus on the situation in which vortex shedding occurs at S_M, we use the terms "synchronization" and "postsynchronization" to refer to this situation.

Variation of the rms C_L with S_M is shown in Fig. 6. The results are presented in terms of relative values, thus the rms C_L is presented relative to its value in the case of $A_x=0$. Similarly, we use the ratio S_M/S_K to express changes in S_M. The lift reduction is clear in this figure, the relative rms C_L is reduced by two orders of magnitude from 1.696 at S_M/S_K =1.80 to 0.0087 (a reduction of 99.5%) at the critical $S_M/S_K=1.81$, which corresponds to the beginning of synchronization.

We decompose the steady-state $C_D(t)$ into a constant mean component $\langle C_D \rangle$ and an oscillatory component $C_{D,osc}$ and analyze each one separately. Variation of the relative mean C_D with S_M/S_K is shown in Fig. 7. Synchronization of the drag causes a reduction in its mean value from 1.32 to 0.77 (a reduction of 42%). In the postsynchronization cases, $\langle C_D \rangle$ is independent of S_M, in contrast with $C_{D,osc}$ whose rms value grows monotonically with S_M as shown in Fig. 8. This growth can be represented by a quadratic function, as indicated in Fig. 9.

B. Mechanical work and drag phase

The nondimensional mechanical work done by the cylinder on the flow per motion cycle T_M (starting from an arbitrary time t_o) is
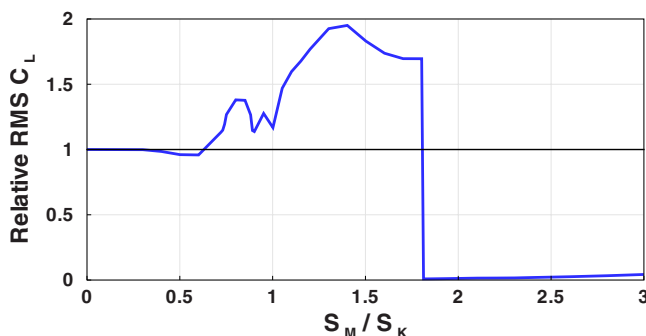

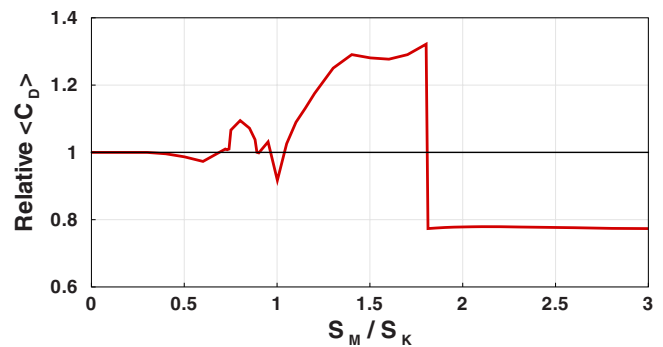FIG. 6. (Color online) Variation of the relative rms C_L with the forcing-to-Strouhal frequency ratio S_M/S_K.

FIG. 7. (Color online) Variation of the relative mean drag coefficient $\langle C_D \rangle$ with the forcing-to-Strouhal frequency ratio S_M/S_K.
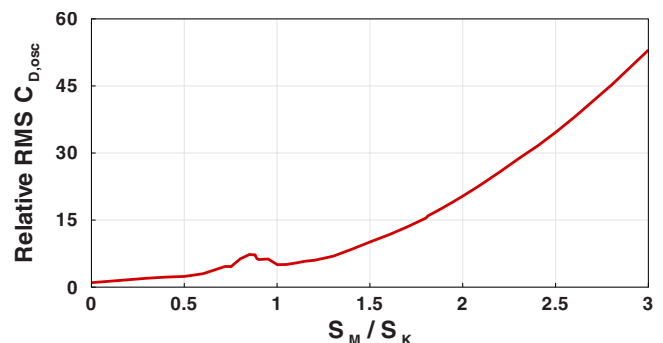

FIG. 8. (Color online) Variation of the relative rms $C_{D,osc}$ with the forcing-to-Strouhal frequency ratio S_M/S_K.

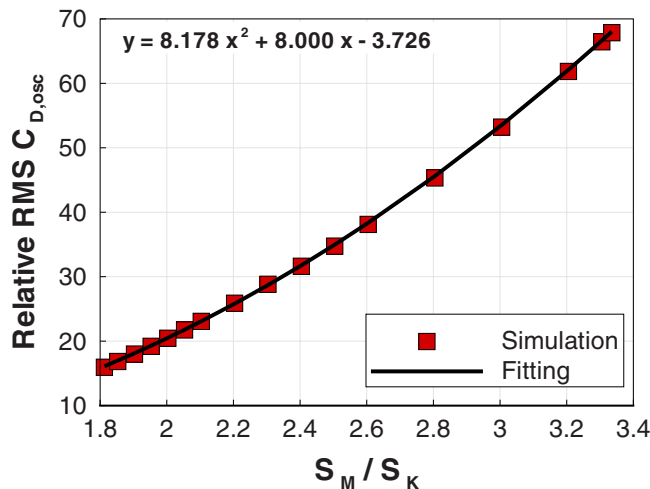FIG. 9. (Color online) Variation of the calculated and fitted relative synchronous rms C_D with the forcing-to-Strouhal frequency ratio S_M/S_K.

$$W_{\text{cyc}} = -A_x 2\pi S_M \int_{t_o}^{t_o+T_M} C_D(t)\cos(2\pi S_M t)dt. \qquad (3)$$

The minus sign on the right-hand side of Eq. (3) ensures the correct sign for W_{cyc} so that, when the velocity of the cylinder and the drag force are in the same direction, W_{cyc} is negative and the work is actually done by the flow on the cylinder. We carry out the above integration numerically using the trapezoidal rule. The results of W_{cyc} as a function of S_M/S_K are given in Fig. 10. The sign of W_{cyc} is always positive, indicating that work is being done by the cylinder on the flow. This constitutes another difference from the case of cross-flow motion, where W_{cyc} takes on both negative and positive values, depending on S_M.

To first order, the steady-state synchronous drag can be approximated as

$$C_D(t) = \langle C_D \rangle + |C_{D,\text{osc}}|\sin(2\pi S_M t + \beta), \qquad (4)$$

where $|.|$ indicates an amplitude and β indicates the phase angle by which C_D leads ξ. Substituting Eqs. (4) and (1) into Eq. (3) leads to the following expression:

$$W_{\text{cyc}} = -\pi A_x |C_{D,\text{osc}}|\sin(\beta). \qquad (5)$$

Equation (5) implies that β must be negative in order to have positive W_{cyc}. We computed β for the synchronous-drag
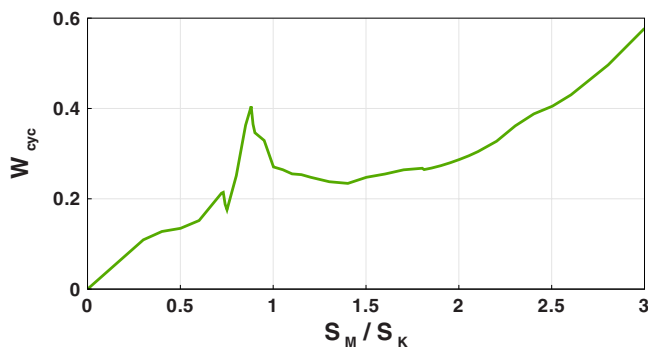
cases and found that it is always negative varying from -0.262 ($-15°$) to -0.175 ($-10°$), as shown in Fig. 11. For cross-flow motion, a sudden change in the phase between the synchronous lift and the motion was reported in different studies;[28–31] we also found it to occur with the current Re and motion amplitude. Such a feature does not occur with the examined in-line motion.

C. Dissipation

We compute the average dissipated power in the flow at each mechanical frequency. Its dimensional expression is

$$\hat{P}_{\text{ave}} = \frac{1}{\hat{t}_2 - \hat{t}_1}\int_{\hat{t}_1}^{\hat{t}_2} \hat{F}_x[\hat{U}_\infty - \dot{\hat{x}}]d\hat{t}, \qquad (6)$$

where $\hat{F}_x$ is the dimensional drag force, $\hat{t}_1$ and $\hat{t}_2$ are arbitrary (but appropriate for statistical analysis), and $[\hat{U}_\infty - \dot{\hat{x}}]$ is the relative velocity between the cylinder and free-stream fluid in the $\hat{F}_x$ direction. Combining Eqs. (1) and (6) yields the following nondimensional expression for the average dissipated power:

$$P_{\text{ave}} = \frac{1}{t_2 - t_1}\int_{t_1}^{t_2} C_D(t)[1 - A_x 2\pi S_M \cos(2\pi S_M t)]dt. \qquad (7)$$

We use at least 40 motion periods to evaluate the integrand in Eq. (7). When $A_x=0$, P_{ave} reduces to $\langle C_D \rangle$. In Fig. 12, variation of the relative P_{ave} with S_M/S_K is shown. Over the
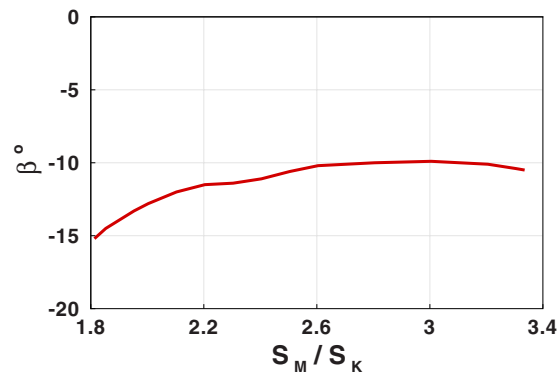

FIG. 11. (Color online) Variation of the phase angle β of the synchronous C_D relative to the nondimensional displacement ξ with the forcing-to-Strouhal frequency ratio S_M/S_K.

FIG. 10. (Color online) Variation of the mechanical work W_{cyc} with the forcing-to-Strouhal frequency ratio S_M/S_K.
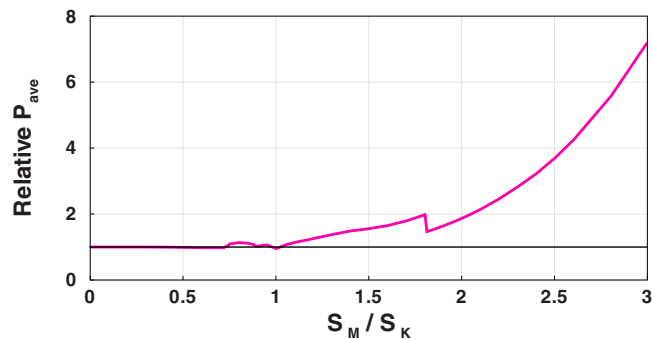

FIG. 12. (Color online) Variation of the relative average dissipated power P_{avg} with the forcing-to-Strouhal frequency ratio S_M/S_K.
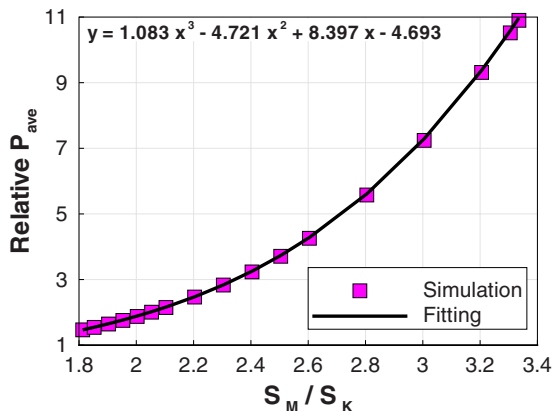
FIG. 13. (Color online) Variation of the calculated and fitted relative average dissipated power P_{avg} with the forcing-to-Strouhal frequency ratio S_M/S_K for synchronous cases.

presynchronization frequencies, P_{ave} increases slowly, whereas it increases quickly with a cubic profile over the postsynchronization frequencies, as indicated by the polynomial fit in Fig. 13. This cubic profile can be explained as follows. The first term in the integrand in Eq. (7) gives $\langle C_D \rangle$, which remains unchanged with S_M for postsynchronization cases, as shown in Fig. 7. Therefore, P_{ave} is controlled by the second term in the integrand, in which $C_D(t)$ is multiplied by S_M. Recalling the approximation in Eq. (4), we find that this term becomes $-\sqrt{2\pi} \sin(\beta) A_x S_M \mathrm{rms} C_{D,osc}$, which is proportional to the product of rms $C_{D,osc}$ and S_M. The angle β varies weakly with S_M, as shown in Fig. 11, and rms $C_{D,osc}$ increases quadratically with S_M as shown in Fig. 9; hence P_{ave} increases in a cubic fashion with S_M.

D. Synchronization map

We found that increasing the motion amplitude decreases the critical frequency at which the lift reduction starts. There is a threshold of this amplitude below, which the lift does not exhibit this feature for any mechanical frequency. We found that the threshold here is $A_x=0.157$. Figure 14 shows the locus of the critical conditions in the $A_x - S_M/S_K$ plane, which separates synchronization and nonsynchronization. Similar variations of the lift and drag with S_M take place at other Re. The loci of the critical conditions at Re=500 and 300 are compared in Fig. 15. The locus of the critical conditions when Re=300 is nearly a straight line with a negative slope,
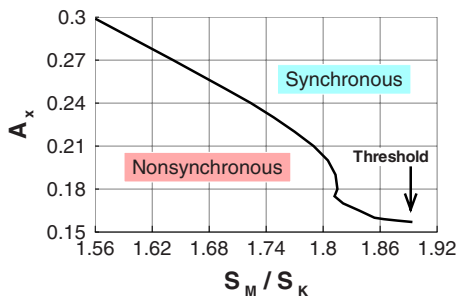

FIG. 14. (Color online) Locus of the critical forcing frequency in the $A_x -S_M/S_K$ plane at Re=500.
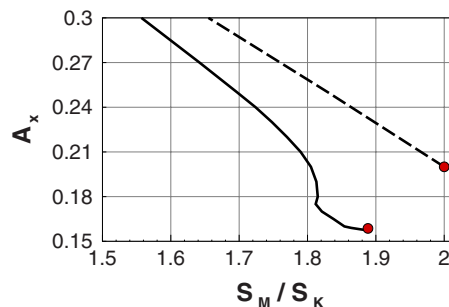

FIG. 15. (Color online) Loci of the critical forcing frequency in the $A_x -S_M/S_K$ plane at Re=500 (solid line) and Re=300 (dashed line). The threshold A_x is indicated by a solid circle.

and the threshold A_x is increased to 0.2. The need for a larger motion amplitude for lift reduction at lower Re can be explained by the higher viscous dissipation. This also explains the absence of such a feature at Re=80 in the experiments of Tanida *et al.*[12] and our simulations.

E. Pre- and postsynchronization modes

In the following part, we present several lift and drag response modes that occur before and after the onset of synchronization. These modes are very different quantitatively and qualitatively. Before the critical frequency, we found lift and drag responses that are either periodic with large period (period-n), quasiperiodic, or chaotic. The best method to distinguish among these responses is Poincaré sections. In Fig. 16, we show representative nonsynchronous cases showing the Poincaré sections of C_L for (i) a quasiperiodic response with $S_M/S_K=0.4$, (ii) a period-6 response with $S_M/S_K=0.72$, (iii) a chaotic response with $S_M/S_K=0.73$, and (iv) a period-2 response with $S_M/S_K=1.7$. The corresponding Poincaré sections of C_D are shown in Fig. 17, which clearly indicate that both of the lift and drag have the same response type for each case.
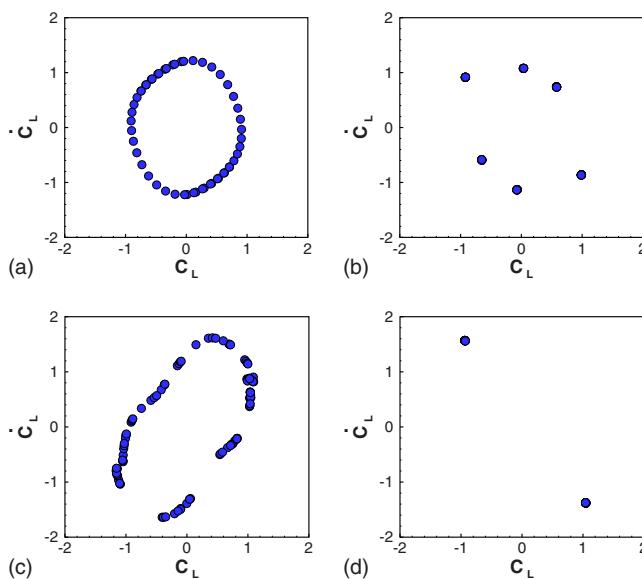

FIG. 16. (Color online) Poincaré sections of nonsynchronous C_L at (i) $S_M/S_K=0.4$, (ii) $S_M/S_K=0.72$, (iii) $S_M/S_K=0.73$, and (iv) $S_M/S_K=1.7$.
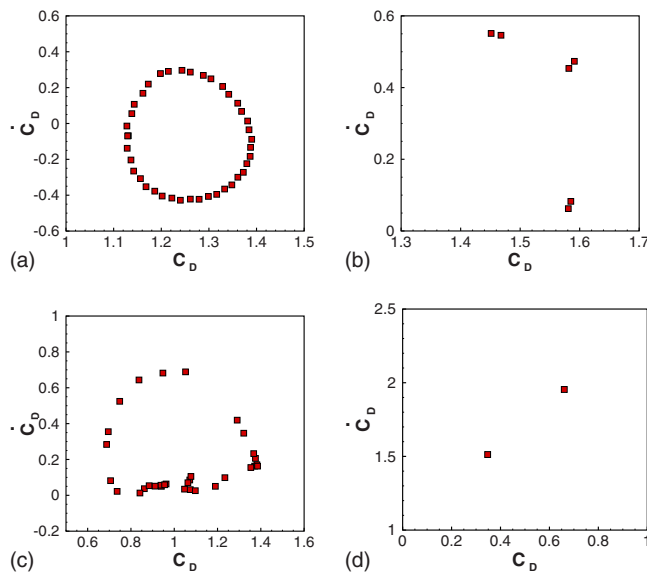
FIG. 17. (Color online) Poincaré sections of nonsynchronous C_D at (i) $S_M/S_K=0.4$, (ii) $S_M/S_K=0.72$, (iii) $S_M/S_K=0.73$, and (iv) $S_M/S_K=1.7$.

The period-2 mode of the lift and drag takes place for a wide range of S_M/S_K (from 1.15 to 1.8). It is followed by synchronization, which is accompanied by large changes in C_L and C_D, as can be seen from comparing the amplitudes and patterns of the time histories for the period-2 case at $S_M/S_K=1.7$ in Fig. 18 to those for the synchronous mode at $S_M/S_K=1.81$ in Fig. 19. The synchronous lift and drag are characterized by a single point in their Poincaré sections, as in Fig. 20. We pay attention to changes that occur in the lift and drag and their coupling due to synchronization. To achieve this, we compare their spectra and cross bicoherence to those we found for the period-2 case at $S_M/S_K=1.7$ (the Poincaré sections of C_L and C_D for this case were shown already in the last plots of Figs. 16 and 17, respectively) and also to those we found for another synchronous case at $S_M/S_K=1$ for a cross-flow motion. The Poincaré sections of C_L and C_D for the latter case are shown in Fig. 21. Whereas each of these sections contains a single point, as was the case in the synchronous cases due to the current in-line motion, we show below that the synchronous C_L is period-1 for both cases and the synchronous C_D is period-1 in case of in-line
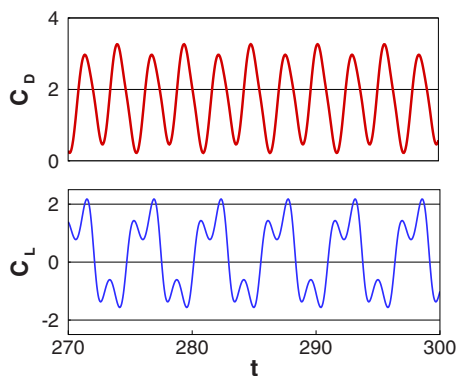
motion but period-$\frac{1}{2}$ in case of cross-flow motion. Because one cannot distinguish between the two cases using the Poincaré sections for C_D, we use second- and third-order spectral analyses to differentiate between them.

The spectra of C_L and C_D for the period-2 case at $S_M/S_K=1.7$ are shown in Fig. 22. The frequency S is scaled with the mechanical frequency S_M to better indicate the positions of the fundamental components and their superharmonics and subharmonics. The fundamental component of C_L is at $\frac{1}{2}S_M$, whereas the fundamental component of C_D is at S_M. There are odd and even superharmonics in the spectrum of C_L, but the odd harmonics are stronger. There are fractional superharmonics in the spectrum of C_D, but the integer ones are stronger. The spectra of C_L and C_D for the synchronous case at $S_M/S_K=1.81$ are shown in Fig. 23. The fundamental component of C_L is now at S_M and the fundamental component of C_D is still at S_M. Whereas there are still even and odd superharmonics in the spectrum of C_L (as in the presynchronization case), their amplitudes decay monotonically and there is no bias toward the odd superharmonics. The fractional superharmonics of C_D have disappeared. The spectra of C_L and C_D for the synchronous case at $S_M/S_K=1$ for cross-flow motion are shown in Fig. 24. One of the main differences between this mode of synchronization and the one due to in-line motion is that C_D is synchronous at $2S_M$ in the case of cross-flow motion rather than at S_M. Also, the spectrum of C_L consists mainly of odd superharmonics, and the spectrum of C_D consists mainly of even ones. It should
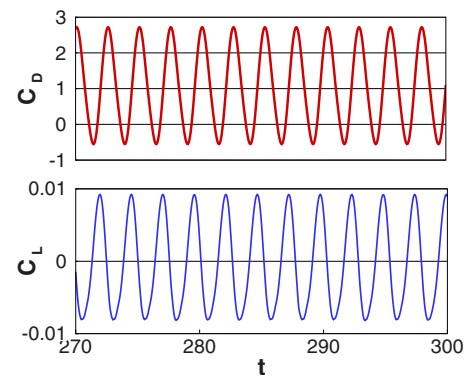

FIG. 19. (Color online) Steady-state time histories of C_L and C_D for the synchronous mode at a forcing-to-Strouhal frequency ratio $S_M/S_K=1.81$.

FIG. 18. (Color online) Steady-state time histories of C_L and C_D for the period-2 mode at a forcing-to-Strouhal frequency ratio $S_M/S_K=1.7$.
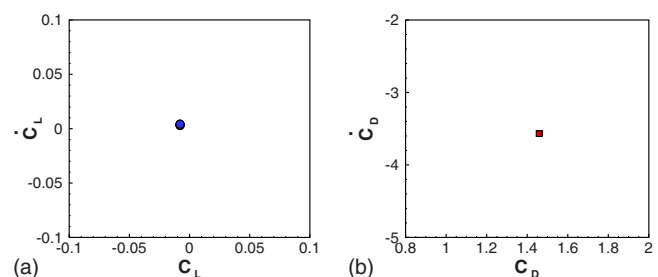

FIG. 20. (Color online) Poincaré sections of C_L and C_D for the synchronous mode due to in-line motion at a forcing-to-Strouhal frequency ratio $S_M/S_K=1.81$.
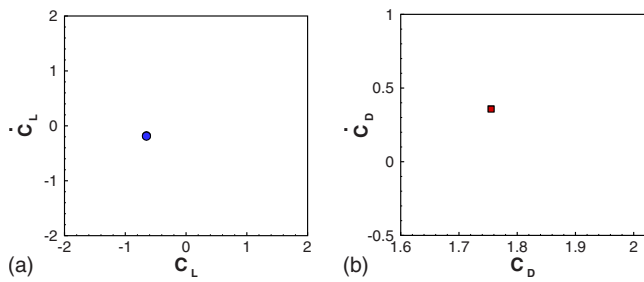
(a)   (b)

FIG. 21. (Color online) Poincaré sections of C_L and C_D for the synchronous mode due to cross-flow motion at a forcing-to-Strouhal frequency ratio $S_M/S_K=1$.

be mentioned here that, in the fixed cylinder case, the spectra of C_L and C_D are qualitatively very similar to those in Fig. 24 (after scaling S with S_K instead of S_M).

If we define a total-force coefficient C_T as $\sqrt{C_L^2+C_D^2}$ and its angular orientation β_T as $\arctan(C_L/C_D)$, which is measured in the counterclockwise direction from the positive x-axis, then the near-harmonic profiles of both C_T and β_T found in the case of synchronization due to cross-stream motion (as shown in Fig. 25 for $S_M/S_K=1$) or in the absence of motion are totally altered in the case of synchronization due to in-line motion as shown in Fig. 26 for $S_M/S_K=1.81$. In the former cases, the frequency of C_T is equal to $2S_M$ (or $2S_K$), which is twice the frequency of β_T. Also, the angle β_T is limited to the first and fourth quadrants, thus C_D is always positive. With in-line synchronization, the profile of β_T becomes nearly a step function with values equal to $0°$ or $\pm 180°$. This effect is a consequence of the extreme reduction in C_L. The interval when $|\beta_T| \approx 180°$ corresponds to negative C_D.

(a)

(b)

FIG. 23. (Color online) Magnitude power spectra of C_L and C_D for the synchronous mode due to in-line motion at a forcing-to-Strouhal frequency ratio $S_M/S_K=1.81$.

F. Higher-order spectral analysis

To examine the nonlinear coupling between C_L and C_D, we calculate the magnitude-squared cross-bicoherence $b_{\mathrm{LLD}}^2(S_1,S_2)$ as

$$b_{\mathrm{LLD}}^2(S_1,S_2) = \frac{|M_{\mathrm{LLD}}(S_1,S_2)|^2}{M_{\mathrm{LL}}(S_1)M_{\mathrm{LL}}(S_2)M_{\mathrm{DD}}(S_1+S_2)}, \tag{8}$$

where

$$M_{\mathrm{LLD}}(S_1,S_2) = E[\tilde{L}^*(S_1)\tilde{L}^*(S_2)\tilde{D}(S_1+S_2)] \tag{9}$$

is the cross bispectrum, $\tilde{L}(S)$ and $\tilde{D}(S)$ are the discrete Fourier transforms of $C_L(t)$ and $C_D(t)$, respectively, E indicates
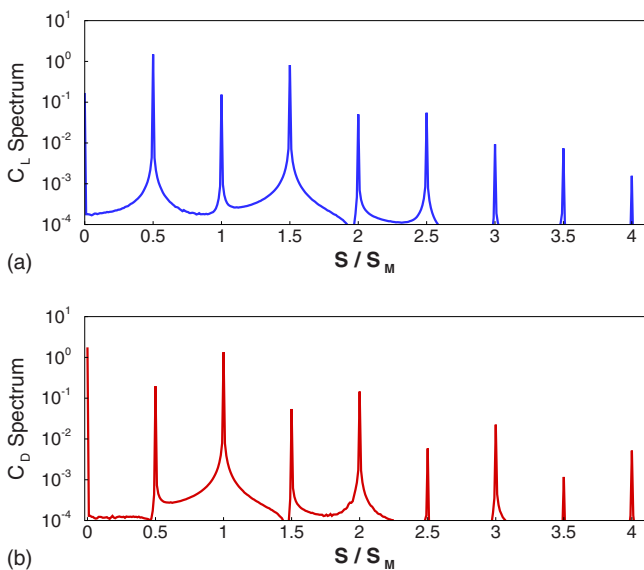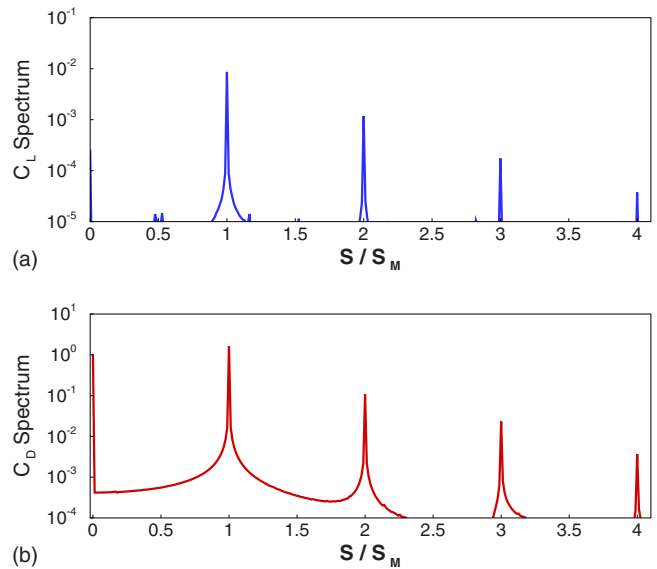

(a)

(b)

FIG. 22. (Color online) Magnitude power spectra of C_L and C_D for the period-2 mode due to in-line motion at a forcing-to-Strouhal frequency ratio $S_M/S_K=1.7$.
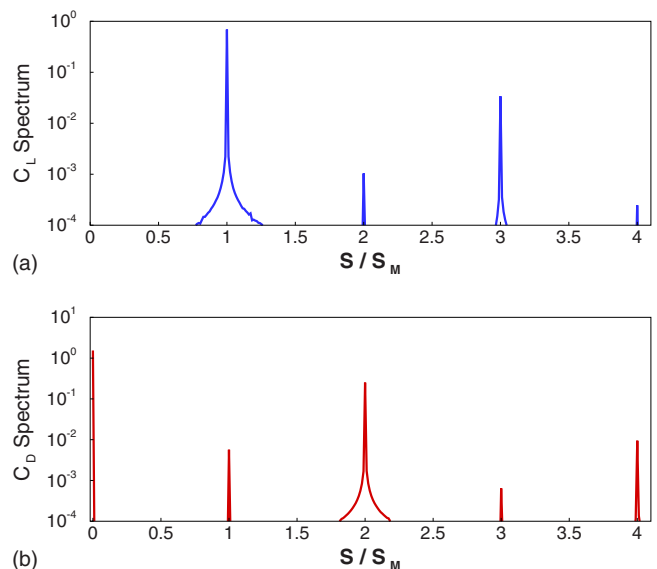

(a)

(b)

FIG. 24. (Color online) Magnitude power spectra of C_D and C_L for the synchronous mode due to cross-flow motion at a forcing-to-Strouhal frequency ratio $S_M/S_K=1$.
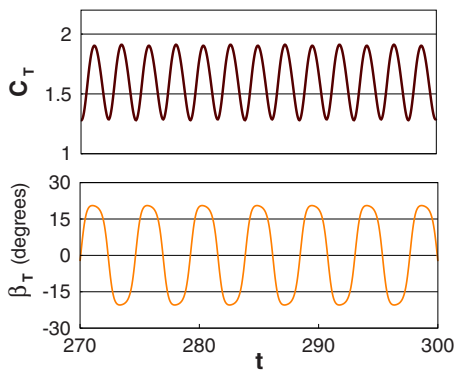
FIG. 25. (Color online) Steady-state time histories of C_T and β_T for the synchronous mode due to cross-flow motion at a forcing-to-Strouhal frequency ratio $S_M/S_K=1$.

FIG. 27. (Color online) Magnitude-squared cross bicoherence for the period-2 mode due to in-line motion at a forcing-to-Strouhal frequency ratio $S_M/S_K=1.7$.

the expected value (or time average), and the superscript $*$ indicates a complex conjugate. The autopower spectra $M_{LL}(f)$ and $M_{DD}(f)$ of C_L and C_D are given by

$$M_{LL}(S) = E[\tilde{L}^*(S)\tilde{L}(S)], \tag{10}$$

$$M_{DD}(S) = E[\tilde{D}^*(S)\tilde{D}(S)]. \tag{11}$$

The corresponding magnitude-squared cross bicoherence for the C_L and C_D spectra in Fig. 22 is shown in Fig. 27. The presence of many quadratically interacting lift components is noticeable. A fractional subharmonic or superharmonic in C_D at $\frac{1}{2}mS_M$ is formed by quadratic coupling between the C_L components at $(m+k)S_M$ and $-(k+\frac{1}{2}m)S_M$, where $k\geq 0$ is an integer. These coherence points are located in the difference region of b_{LLD}^2. They are in addition to other couplings between the C_L components at $(\frac{1}{2}m-k)S_M$ and kS_M, where $k>0$ is an integer. These coherence points are located in the sum region of b_{LLD}^2. The number of coherence points is reduced in the synchronized cases, as shown in Fig. 28, which corresponds to the spectra of C_L and C_D in Fig. 23. This is because there are phase-coherent components at fractions of S_M. The fundamental frequency of C_D at S_M is formed by the interaction of the components of C_L at kS_M and $-(k+1)S_M$, where $k\geq 0$ is an integer. Similarly, the superharmonic in the spectrum of C_D at $2S_M$ is formed by the interaction of components of C_L at kS_M and $-(k+2)S_M$ in addition to self-

interacting C_L component at S_M. A similar structure occurs for the higher superharmonics in C_D. The bicoherence plot is even simplified further for synchronization cases due to cross-flow motion, as shown in Fig. 29, which corresponds to the C_L and C_D spectra in Fig. 24. This is because of the presence of half the number of significant superharmonics in the C_L (odd ones) and C_D (even ones) spectra. The fundamental component of C_D at $2S_M$ is formed by self-interacting C_L component at S_M in addition to the interaction of the components of C_L at $3S_M$ and $-S_M$. The small C_D subharmonic at S_M is formed by the interaction of the components of C_L at $2S_M$ and $-S_M$.

The bicoherence analysis provides information about the quadratic coupling of the C_L components in the C_D components. To examine the linear correlation between the C_L and C_D components, we use the (linear) cross-power spectrum $M_{LD}(f)$, defined as

$$M_{LD}(S) = E[\tilde{L}^*(S)\tilde{D}(S)]. \tag{12}$$

Figures 30–32 show the absolute value of the cross-power spectrum $|M_{LD}(S)|$ corresponding to the C_L and C_D spectra in Figs. 22–24, respectively. For the presynchronization case, $|M_{LD}(S)|$ in Fig. 30 indicates that all C_L components have linear coupling with the respective C_D components. The couplings at $\frac{1}{2}S_M$ and S_M are both one order of magnitude larger than the one at the subsequent superharmonic at $\frac{3}{2}S_M$. For the synchronized cases with either in-line or cross-flow motion,
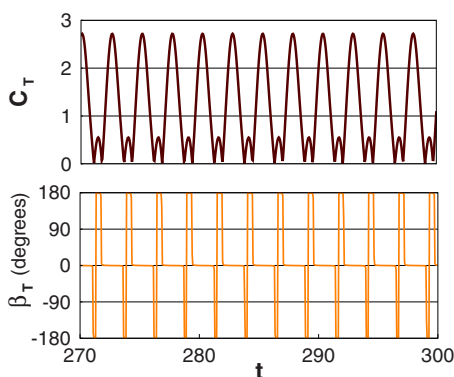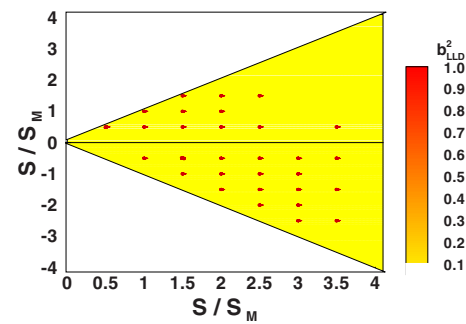

FIG. 26. (Color online) Steady-state time histories of C_T and β_T for the synchronous mode due to in-line motion at a forcing-to-Strouhal frequency ratio $S_M/S_K=1.81$.
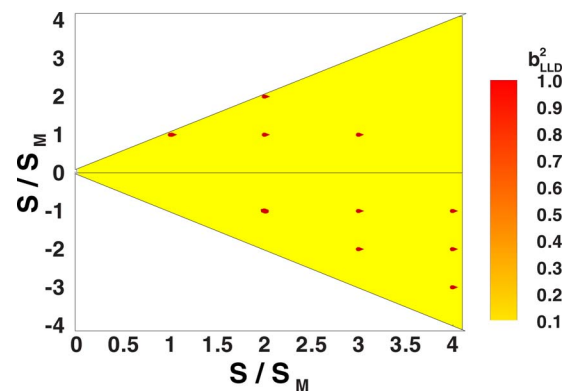

FIG. 28. (Color online) Magnitude-squared cross bicoherence for the synchronous mode due to in-line motion at a forcing-to-Strouhal frequency ratio $S_M/S_K=1.81$.
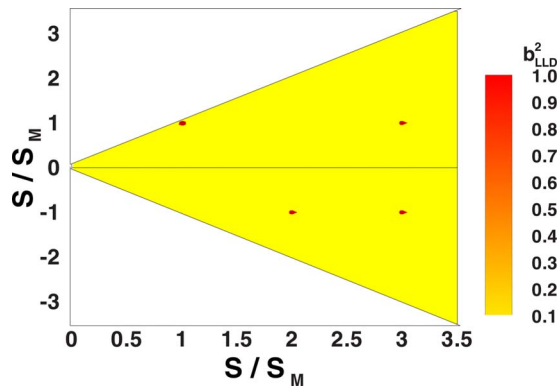
FIG. 29. (Color online) Magnitude-squared cross bicoherence b_{LLD}^2 for the synchronous mode due to cross-flow motion at a forcing-to-Strouhal frequency ratio $S_M/S_K=1$.

FIG. 31. (Color online) Absolute of cross-power spectrum $|M_{\text{LD}}|$ for the synchronous mode due to in-line motion at a forcing-to-Strouhal frequency ratio $S_M/S_K=1.81$.

linear couplings occur at S_M and its integer superharmonics. The decay of $|M_{\text{LD}}(S)|$ at higher superharmonics is faster in the case of in-line motion.

G. Wake structure

In the remaining part of this study, we relate the large differences in the postsynchronization cases, including the significant lift reduction and the saturation of the mean drag, to changes in the vortex shedding and the pressure distribution on the surface of the cylinder. In Fig. 33, vorticity contours in the near field for two postsynchronization cases (at $S_M/S_K=1.81$ and 3) are shown at the instant when $\xi(t)=0$ and increasing (from negative to positive), and therefore $\dot{\xi}$ is maximum. The typical von Kármán vortex street with $2S$ mode is replaced by two parallel $1S$ streets: one with positive vortices located behind the bottom point of the surface and the other with negative vortices located behind its top point. This instantaneous symmetry in the wake is what causes the reduction in C_L because the lift force is a result of the instantaneous imbalance in the surface pressure (which is related to the vortex strength at the surface) between the top and bottom parts of the surface. As S_M increases, the vortex shedding frequency also increases and the shed vortices along each street become closer and those being shed from the surface become stronger (higher vorticity levels). So, we expect more negative pressure at the locations of these vortices on the surface of the cylinder.
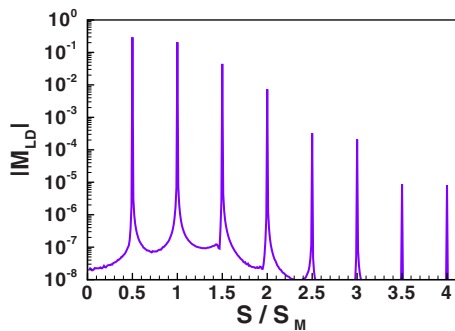
In the classical vortex shedding mechanism for a fixed cylinder, two contrarotating vortices are periodically formed and shed downstream in the wake. This is due to the shear-layer instability, which causes vortex roll-up and leads to the generation of an upper vortex and lower vortex in a periodic and staggered pattern. The lift frequency is equal to the shedding frequency but the drag frequency is equal to twice the shedding frequency because both upper and lower vortices contribute to the drag through the changes they induce in the pressure field. This shedding mechanism is preserved in the case of a synchronous wake due to cross-flow oscillation, which is expected because the wake structure remains similar to the one taking place in the case of a fixed cylinder, and the effect of the shear-layer instability is not inhibited by the cross-flow oscillation. Consequently, either the upper or lower vortex still contributes to the drag, keeping its frequency twice the frequency of the shedding and lift. On the other hand, the in-line oscillation influences the locations and motions of the formed vortices, which tend to oppose the cylinder motion due to the added-mass effect. When the cylinder velocity is strong enough, which corresponds to a high frequency or high amplitude, this disturbing influence of the oscillation overpowers the effect of the shear-layer instability and becomes the dominant mechanism that controls the vortex formation and shedding. This results in a sudden change in the wake state, causing it to be instantaneously symmetric and consequently reduces the lift dramatically. The vortices are no longer staggered, but they are convected parallel to

FIG. 30. (Color online) Absolute of cross-power spectrum $|M_{\text{LD}}|$ for the period-2 mode due to in-line motion at a forcing-to-Strouhal frequency ratio $S_M/S_K=1.7$.
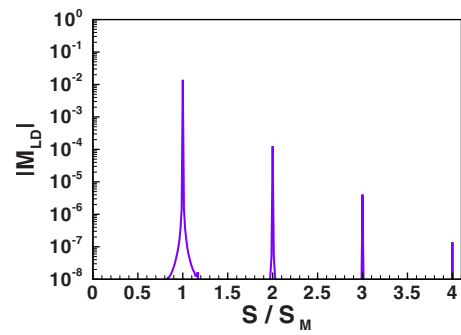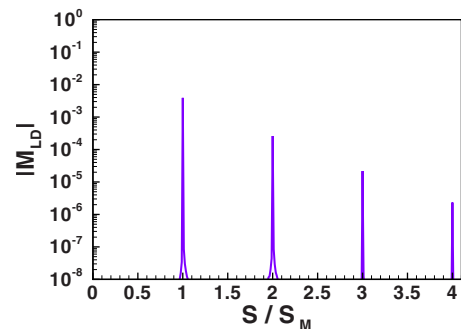

FIG. 32. (Color online) Absolute of cross-power spectrum $|M_{\text{LD}}|$ for the synchronous mode due to cross-flow motion at a forcing-to-Strouhal frequency ratio $S_M/S_K=1$.
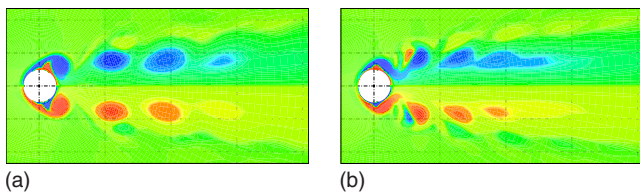
FIG. 33. (Color online) Vorticity contours when $\xi=0$ for synchronous cases: (i) $S_M/S_K=1.81$ and (ii) $S_M/S_K=3$. Positive (counterclockwise) vortex is being shed from the bottom surface.

each other, which causes the drag frequency to be equal to the shedding frequency because both vortices contribute simultaneously to the drag. This explanation is supported by the four vorticity contours in Fig. 34 that are taken over one cycle of in-line motion, separated in time by a quarter cycle, for the postsynchronization case at $S_M/S_K=1.81$. The corresponding surface distributions of the pressure coefficient are shown and discussed in Sec. III H, which are in support of the mentioned change in the drag frequency. This explanation is also justified by our finding that the critical frequency, at which the wake state changes, decreases with the oscillation amplitude as shown in the synchronization maps in Figs. 14 and 15. Therefore, the combined effect of the frequency and amplitude of the cylinder motion is what drives the change in the wake state. Barbi *et al.*[32] experimentally perturbed the inflow velocity rather than the in-line motion of the cylinder. Therefore, the constant velocity $\hat{U}_\infty$ of the incoming stream is replaced by an oscillating one, which has a nonzero mean value. Although the perturbation mechanism of the shedding is different from the one we implement here, the Reynolds number is higher (3000–40 000), the aspect ratios of the cylinders used are low (including a length-to-diameter ratio of 2.5), and the perturbation could not be made purely harmonic, they found cases where shedding occurs at the pulsation frequency. It is interesting that, for this case, the lift and drag have the same frequencies, the lift is remarkably reduced, and two vortices are symmetrically shed every perturbation cycle. These features are similar to the ones we found in our study, which covered a wider range of frequencies

H. Surface pressure

Figure 35 shows distributions of the mean pressure coefficient $\langle C_P \rangle$ at the cylinder surface for the same two postsynchronization cases shown in Fig. 33. The distributions in this figure are almost symmetric about the base point (where the angular coordinate θ is 180°), which causes the mean C_L to be zero. Whereas this figure cannot reveal much about the large reduction in the rms C_L due to synchronization, we use it to interpret the reduction and saturation behavior of the mean C_D due to synchronization. The value of $\langle C_D \rangle$ is mainly due to the imbalance in $\langle C_P \rangle$ between the upstream and downstream parts of the surface. The upstream $\langle C_P \rangle$ is close to unity, whereas the downstream $\langle C_P \rangle$ is negative. We recall that the part of the surface near the base point ($\theta = 180°$) is nearly isolated from shed vortices in the postsynchronization cases, as shown in Fig. 33. This is reflected in
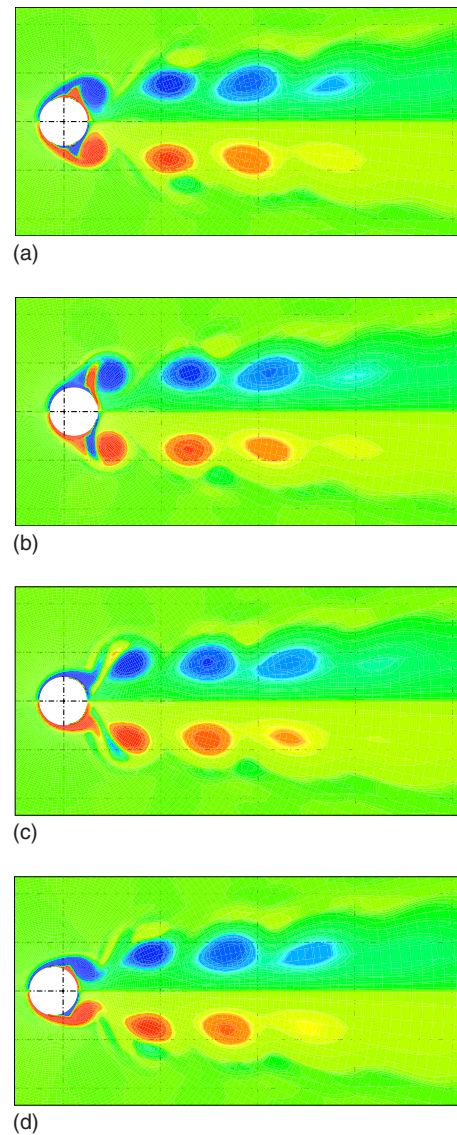

(a)

(b)

(c)

(d)

FIG. 34. (Color online) Vorticity contours over one motion cycle for $S_M/S_K=1.81$. The motion sequence is (i) $\xi=0$ and $\dot{\xi}$ is maximum, (ii) ξ is maximum and $\dot{\xi}=0$, (iii) $\xi=0$ and $\dot{\xi}$ is minimum, and (iv) ξ is minimum and $\dot{\xi}=0$. Positive (counterclockwise) vortex is being shed from the bottom surface.

the "bump" in the downstream $\langle C_P \rangle$ at $S_M/S_K=1.81$; it explains the 42% reduction in $\langle C_D \rangle$ once synchronization occurs. To interpret the saturation behavior, we compare the two surface distributions of $\langle C_P \rangle$ at $S_M/S_K=1.81$ and 3. The downstream bump is stronger in the latter case, which should result in a reduced $\langle C_D \rangle$ for this high-frequency synchronized
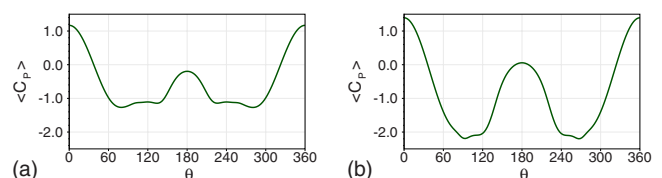

FIG. 35. (Color online) Surface distribution of $\langle C_P \rangle$ for synchronous cases: (i) $S_M/S_K=1.81$ and (ii) $S_M/S_K=3$. The angle θ is 0 at the stagnation point and 90° at the top point.
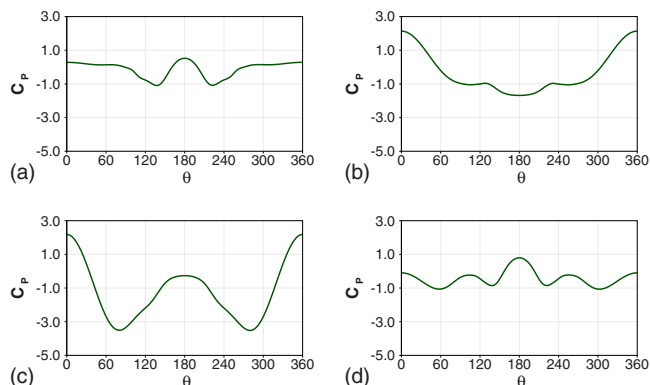
FIG. 36. (Color online) Surface distribution of C_P over one motion cycle for $S_M/S_K=1.81$. The motion sequence is (i) $\xi=0$ and $\dot{\xi}$ is maximum, (ii) ξ is maximum and $\dot{\xi}=0$, (iii) $\xi=0$ and $\dot{\xi}$ is minimum, and (iv) ξ is minimum and $\dot{\xi}=0$.

case. However, this is counteracted to a large extent by a reduction (more negative) in $\langle C_P \rangle$ over $\theta=30°-90°$ and $270°-360°$. Therefore, variations in $\langle C_D \rangle$ for the postsynchronization cases are minimal.

To support and augment the above discussion on C_L, C_D, and surface $\langle C_P \rangle$, we examine the surface distributions of C_P over one motion cycle for the postsynchronization case at $S_M/S_K=1.81$ in Fig. 36. The surface C_P is shown at four equally spaced instants of time. The surface C_P exhibits instantaneous symmetry about the x-axis. This is due to the instantaneous symmetry of the magnitude of the vorticity at the surface. Because the peaks and valleys in $C_L(t)$ are mainly due to the difference between C_P at the top and bottom parts of the surface, these peaks and valleys are reduced in the postsynchronization cases due to the strong reduction in the C_P difference that contributes to $|C_L|$. These C_P snapshots also explain the increase in rms $C_{D,\text{osc}}$ with S_M for the postsynchronization cases even though $\langle C_D \rangle$ remains unchanged. Because the surface distribution of $\langle C_P \rangle$ becomes more distorted as S_M increases (as in Fig. 35), the distortion in the instantaneous C_P distributions is strengthened also. The rms $C_{D,\text{osc}}$ depends on the instantaneous C_P imbalance between the upstream and downstream parts of the surface. This imbalance increases steadily with S_M as a result of the intensified vorticity at the surface.

IV. CONCLUSIONS

We studied the dynamics of the loads on a cylinder undergoing harmonic in-line motion in a uniform stream at different nondimensional mechanical frequencies S_M and amplitudes A_x using the computational fluid dynamics (CFD) method. For a given Reynolds number Re, there exists a curve in the A_x-S_M plane above which synchronization occurs. In the absence of synchronization, the lift and drag can be periodic with large period, quasiperiodic, or chaotic. Synchronization occurs at lower values of S_M when either A_x or Re increases. When synchronization takes place, the lift and drag are both synchronous with S_M, the lift has almost zero amplitude, the mean drag drops and saturates at a constant value regardless of S_M, its rms grows quadratically with S_M,

the wake structure and shedding change and become instantaneously symmetric, and the coupling between the lift and drag changes. Whereas the linear coupling between the synchronous lift and drag is similar for the in-line and cross-flow motions, their quadratic coupling is different. The drag has an exciting effect for all cases, synchronous or not, and the mechanical work due to the drag and the motion is done on the flow and not on the cylinder. The instantaneous symmetry in the vortex structure affects the surface distribution of the pressure, which in turn explains the qualitative and quantitative changes in the lift and drag when they become synchronous.

[1]G. V. Parkinson, "Mathematical models of flow-induced vibrations of bluff bodies," IUTAM/IAHK Symposium on Flow-Induced Structural Vibrations, Karlsruhe, Germany, 1972, pp. 81–127.
[2]G. Di Silvio, F. Angrilli, and A. Zanardo, "Fluidelastic vibrations: Mathematical model and experimental result," Meccanica **10**, 269 (1975).
[3]T. Sarpkaya, "Fluid forces on oscillating cylinders," J. Wtrwy., Port, Coast., and Oc. Div. **104**, 275 (1978).
[4]G. H. Koopmann, "The vortex wakes of vibrating cylinders at low Reynolds numbers," J. Fluid Mech. **28**, 501 (1967).
[5]S. Krishnamoorthy, S. J. Price, and M. P. Païdoussis, "Cross-flow past an oscillating circular cylinder: Synchronization phenomena in the near wake," J. Fluids Struct. **15**, 955 (2001).
[6]O. A. Marzouk and A. H. Nayfeh, "A study of the forces on an oscillating cylinder," Proceedings of the 26th International Conference on Offshore Mechanics and Arctic Engineering, San Diego, CA, 2007, Vol. 3, pp. 741–752.
[7]O. A. Marzouk and A. H. Nayfeh, "Loads on a harmonically oscillating cylinder," Proceedings of ASME International Design Engineering Technical Conferences and Computers and Information in Engineering Conference, Las Vegas, NV, 2007.
[8]H. Persillon and M. Braza, "Physical analysis of the transition to turbulence in the wake of a circular cylinder by three-dimensional Navier–Stokes simulation," J. Fluid Mech. **365**, 23 (1998).
[9]A. H. Nayfeh, F. Owis, and M. R. Hajj, "A model for the coupled lift and drag on a circular cylinder," Proceedings of ASME International Design Engineering Technical Conferences and Computers and Information in Engineering Conference, Chicago, IL, 2003.
[10]A. H. Nayfeh, O. A. Marzouk, H. N. Arafat, and I. Akhtar, "Modeling the transient and steady-state flow over a stationary cylinder," Proceedings of ASME International Design Engineering Technical Conferences and Computers and Information in Engineering Conference, Long Beach, CA, 2005.
[11]M. Tatsuno, "Vortex street behind a circular cylinder oscillating in the stream direction," Bulletin of Research Institute for Applied Mechanics, Kyushu University **36**, 25 (1972).
[12]Y. Tanida, A. Okajima, and Y. Watanabe, "Stability of a circular cylinder oscillating in uniform flow or in a wake," J. Fluid Mech. **61**, 769 (1973).
[13]O. M. Griffin and S. E. Ramberg, "Vortex shedding from a cylinder vibrating in line with an incident uniform flow," J. Fluid Mech. **75**, 257 (1976).
[14]A. Leonard and A. Roshko, "Aspects of flow-induced vibration," J. Fluids Struct. **15**, 415 (2001).
[15]R. D. Gabbai and H. Benaroya, "An overview of modeling and experiments of vortex-induced vibration of circular cylinders," J. Sound Vib. **282**, 575 (2005).
[16]L. E. Ericsson, "Karman vortex shedding and the effect of body motion," AIAA J. **18**, 935 (1980).
[17]A. Ongoren and D. Rockwell, "Flow structure from an oscillating cylinder Part 1. Mechanisms of phase shift and recovery in the near wake," J. Fluid Mech. **191**, 197 (1988).
[18]M. Gaydon and D. Rockwell, "Vortices incident upon an oscillating cylinder: Flow structure and loading," J. Fluids Struct. **13**, 709 (1999).
[19]Y. Constantinides and O. H. Oakley, Jr., "Numerical prediction of bare and straked cylinder VIV," Proceedings of the 25th International Conference on Offshore Mechanics and Arctic Engineering, Hamburg, Germany, 2006.
[20]J. K. Vandiver, "The relationship between in-line and cross-flow vortex-induced vibration in cylinder," J. Fluids Struct. **1**, 381 (1987).

[21] A. Torum, G. Moe, J. V. Johansen, and E. Katla, "On current induced in-line motion in pipelines free-spans," Proceedings of the 15th International Conference on Offshore Mechanics and Arctic Engineering, Florence, Italy, 1996, Vol. 5, pp. 459– 469.

[22] R. Korpus, P. Jones, O. Oakley, and L. Imas, "Prediction of viscous forces on oscillating cylinders by Reynolds-averaged Navier–Stokes solver," Proceedings of the 10th International Offshore and Polar Engineering Conference, Seattle, WA, 2000.

[23] N. Jauvtis and C. H. K. Williamson, "Vortex-induced vibration of a cylinder with two degrees of freedom," J. Fluids Struct. **17**, 1035 (2003).

[24] L. Lee, D. Allen, J. P. Pontaza, F. Kopp, and V. Jhingran, "In-line motion of subsea pipeline span models experiencing vortex-shedding," Proceedings of the 28th International Conference on Ocean, Offshore Arctic Engineering, Honolulu, Hawaii, 31 May–5 June, 2009.

[25] B.-H. Kim and D. R. Williams, "Nonlinear coupling of fluctuating drag and lift on cylinders undergoing forced oscillations," J. Fluid Mech. **559**, 335 (2006).

[26] J. F. Thompson, Z. U. A. Warsi, and C. W. Mastin, *Numerical Grid Generation* (Elsevier Science Publishers, New York, 1985).

[27] K. A. Hoffmann and S. T. Chiang, *Computational Fluid Dynamics for Engineers*, 4th ed. (Engineering Education System, Wichita, KS, 2000), Vol. 2.

[28] O. A. Marzouk and A. H. Nayfeh, "Detailed characteristics of the resonating and non-resonating flows past a moving cylinder," Proceedings of the 16th AIAA/ASME/AHS Adaptive Structures Conference, Schaumburg, IL, 2008.

[29] M. M. Zdravkovich, "Modification of vortex shedding in the synchronization range," ASME J. Fluids Eng. **104**, 513 (1982).

[30] T. Staubli, "Calculation of the vibration of an elastically mounted cylinder using experimental data from forced vibration," ASME J. Fluids Eng. **105**, 225 (1983).

[31] X. Lu and C. Dalton, "Calculation of the timing of vortex formation from an oscillating circular cylinder," J. Fluids Struct. **10**, 527 (1996).

[32] C. Barbi, D. P. Favier, C. A. Maresca, and D. P. Telionis, "Vortex shedding and lock-on of a circular cylinder in oscillatory flow," J. Fluid Mech. **170**, 527 (1986).